NASA Contractor Report 4756

Validation Tests of TASS for Application to 3-D Vortex Simulations

George F. Switzer
Research Triangle Institute • Research Triangle Park, North Carolina

National Aeronautics and Space Administration
Langley Research Center • Hampton, Virginia 23681-0001

Prepared for Langley Research Center
under Contract NAS1-18925

October 1996

Table of Contents

List of Figures ii

List of Tables iii

Abstract 1

1.0 Introduction 2
1.1 Purpose 2
1.2 Overview of Documentation 3

2.0 TASS Model Description 4
2.1 Tass Equation Set 5
2.2 TASS Equation Set Reduced for Beltrami Flow Simulations 6

3.0 TASS Numerics 7
3.1 Time derivative 7
3.2 Space Derivative 8
3.3 FIlter 8

4.0 Viscous Beltrami Flow 10

5.0 Initialization Conditions for the Validation Case of the TASS Code 13

6.0 TASS Run Results 14
6.1 Baseline Test Case 14
6.1.1 Comparison of TASS with ARPS 14
6.2 Additional TASS Runs 15
6.2.1 Spatial Accuracy 19
6.2.2 Temporal Accuracy 20
6.2.3 Fourth-Order Filter 22
6.2.4 Comparison of ARPS to TASS with Fourth-Order Spatial Accuracy 23

7.0 Conclusion 24

Acknowledgments 25

8.0 References 26

9.0 Figures 28

List of Figures

Figure 1: Initial Beltrami flow field 2-D vector plots. Horizontal plane at mz = π/2 (top), vertical East-West Plane at ly = π (middle), and vertical North-South plane at kx = π (bottom). 28

Figure 2: Perspective of North-South vertical planes of vectors at kx = 0,π,2π,3π and 4π. 29

Figure 3: Analytical time history of total kinetic energy and maximum velocity for viscously decaying Beltrami flow (ν=1 m2/s). 30

Figure 4: Comparison of TASS (top) and ARPS (bottom) horizontal velocity error plots at mz = π/2. 31

Figure 5: Comparison of TASS (top) and ARPS (bottom) horizontal vertical velocity error contour plots at mz = π/2. 32

Figure 6: Time history of kinetic energy (top) and vertical velocity (bottom) percent error for decaying case runs. 33

Figure 7: Time history of kinetic energy (top) and vertical velocity (bottom) percent error for weakly-decaying case runs (runs 7 and 9 are identical). 34

Figure 8: Spatial second-order (top) and fourth-order (bottom) horizontal TASS velocity error vector plots at mz = π/2. 35

Figure 9: Spatial second-order (top) and fourth-order (bottom) horizontal TASS vertical velocity error contour plot at mz = π/2. 36

Figure 10: Temporal MAB scheme (top) and AB scheme (bottom) horizontal TASS velocity error vector plot at mz = π/2. 37

Figure 11: Temporal MAB scheme (top) and AB scheme (bottom) horizontal TASS vertical velocity error contour plot at mz = π/2. 38

Figure 12: Horizontal vertical velocity error contour plot at mz = π/2 for TASS with fourth-order spatial advection (top) and ARPS (bottom). 39

List of Tables

Table 2.1: TASS 6.x Salient Characteristics (from Proctor 1996) 5

Table 3.1: TASS 6.x Numerics 7

Table 6.1: TASS Run Settings 18

Table 6.2: TASS Run Results 18

Abstract

Direct analytical solutions can be useful in validating the core formulation of numerical systems. In this document an exact analytical solution to the nonlinear Navier-Stokes equation is compared to the numerical results from the three-dimensional Terminal Area Simulation System (TASS). This exact solution, of which the derivation is included, is for Beltrami type flow. Direct comparison of TASS to the analytical Beltrami solution is then used in evaluating the accuracy of TASS.

1.0 Introduction

1.1 Purpose

Numerical simulation of three-dimensional wake vortices needs lengthy time integrations over very large computational domains. Therefore, computational methods are required that are very efficient in the use of computer time and memory, yet are both stable and accurate. Use of numerical schemes with artificial (numerical) diffusion and moderate explicit filtering should be avoided; otherwise, the numerical simulations may be corrupted by artificial dilation of the wake vortex core and unrealistic decay of circulation. This, in turn, may adversely affect the highly-coupled three-dimensional flow of the vortex and may either retard or promote the generation of dynamic instabilities.

A simple approach for evaluating the accuracy and stability of a numerical system is to compare results with analytical solutions. However, exact analytical solutions to the nonlinear three-dimensional Navier-Stokes equations are not simple to find. One such solution is Beltrami flow (Wang 1990, Taylor 1923), a class of flows for which the nonlinear terms are both non-zero and vanish in the vorticity reformulation of the Navier-Stokes equations. Solutions to Beltrami flow yield helical flows having the velocity and the vorticity vectors aligned in the same direction.

Shapiro (1993) presented a solution for viscously-decaying Beltrami flow and its implementation within a non-hydrostatic numerical model called the University of Oklahoma Advanced Regional Prediction System (ARPS). He demonstrated that it could be conveniently applied for validation of three-dimensional numerical models. Shapiro used this analytical Beltrami solution to demonstrate its potential utility in validating other numerical models and, specifically, to evaluate the integrity of the ARPS mode.

TASS has been modified to run Shapiro's analytical Beltrami solution thereby adding to the array of test cases currently used for validation. Beltrami flow simulation adds a unique contribution by testing the model's core formulation for accuracy. This test case also provides a way to check and verify the fundamental numerical approximations in addition to the fidelity of the basic equations set.

1.2 Overview of Documentation

The TASS model is described in Section 2.0. Included in the description is a general overview of the capabilities of TASS along with a description of the TASS base equation set and its simplification resulting from Beltrami flow assumptions. Section 3.0 addresses the salient numerics of TASS important for this investigation. Next in section 4.0 is a derivation of the analytical Beltrami solution. Section 5.0 details the particular parameters used to initialize the Beltrami solution. Section 6.0 then compares TASS results to both ARPS results and the analytical solution. The comparison of TASS results to the analytical Beltrami solution will show the sensitivity of the spatial accuracy, temporal accuracy and the fourth-order filter upon the simulation system.

2.0 TASS Model Description

TASS is a three-dimensional time-dependent, nonhydrostatic, compressible model developed at NASA Langley Research Center for the general purpose of studying convective phenomena such as microbursts/windshear, convective rain storms, gust fronts, hailstorms, and aircraft wake vortices (Proctor, 1987a, 1996). The equations are primitive, non-Boussinesq developed within a meteorological framework. For representative ambient conditions that are supplied as input, TASS has produced simulations of real-world events that are of reasonable comparison with observations (Proctor 1987b, 1993, 1996, Proctor & Bowles, 1992, Proctor et al 1995, Schowalter et al 1995, 1996). The salient characteristics of TASS are listed in table 2.1.

Table 2.1: TASS Salient Characteristics (from Proctor 1996)

Primitive equation / non-Boussinesq equation set: time-dependent, nonhydrostatic, compressible
Meteorological framework with option for either three-dimensional or two-dimensional simulations
Liquid and ice phase microphysics -- can simulate growth processes for cloud droplets, cloud ice crystals, rain, snow, and hail/graupel
Inverse-exponential size distributions for precipitating hydrometeors
Large Eddy Simulation model with first-order subgrid scale turbulence closure -- scales of turbulence larger than grid volume are resolved in the simulation
Ground stress function of surface roughness height
Choice of lateral boundaries: may be either open, mirror, or periodic -- open condition utilizes mass conservative, nonreflective radiation boundary scheme
Option for nonstationary domain -- movable, storm/vortex centering mesh
Explicit numerical schemes, quadratic conservative, time-split compressible -- *accurate and highly efficient, almost no numerical diffusion*
Arakawa C-grid staggered mesh and vertical coordinate stretching allowed
Ambient atmospheric conditions initialized with vertical profile of pressure or altitude, temperature, dew point, and wind velocity
Model applicable to meso-γ and micro-scale atmospheric phenomenon
Initialization modules for simulation of convective storms, microbursts, atmospheric boundary layers, and aircraft wake vortices

2.1 Tass Equation Set

The TASS model contains twelve prognostic equations: three for momentum and one each for pressure deviations and potential temperature, six coupled equations for continuity of water substance (water vapor, cloud droplet, cloud ice crystals, rain, snow, and hail); and one for a massless tracer. The equations governing momentum and pressure in tensor form are (Proctor 1996):

Momentum:

$$\frac{\partial u_i}{\partial t} + \frac{H}{\rho_0}\frac{\partial p}{\partial x_i} = -\frac{\partial u_i u_j}{\partial x_j} + u_i\frac{\partial u_j}{\partial x_j} + g\,(H-1)\,\delta_{i3} - 2\Omega\,(u_k - u_{k0})\,\varepsilon_{ijk} + \frac{1}{\rho_0}\frac{\partial \tau_{ij}}{\partial x_j}\ , \qquad (1)$$

Pressure Deviation:

$$\frac{\partial p}{\partial t} + \frac{C_p P}{C_v}\frac{\partial u_j}{\partial x_j} = \rho_0 g u_j \delta_{j3} + \frac{C_p P}{C_v}\frac{d\theta}{\theta dt}, \tag{2}$$

where, u_i is the tensor component of the velocity, t is time, p is the deviation from atmospheric pressure P, H is the buoyancy term, ρ is the air density, Ω is the earth's angular velocity, g is the earth's gravitational acceleration, θ is the potential temperature, τ_{ij} is the stress tensor, and C_p and C_v are the specific heats of air at constant pressure and volume. Environmental state variables, e.g. u_{k0}, ρ_0, T_0, and θ_0, are defined from the initial input sounding and are functions of height only.

2.2 TASS Equation Set Reduced for Beltrami Flow Simulations

The above equations are simplified for viscous Beltrami flow, since for Beltrami flow: $\rho=\rho_o$=constant, H=1.0, Ω=0, ν_m=constant, and $d\theta/dt$=0, therefore,

Momentum:

$$\frac{\partial u_i}{\partial t} + \frac{1}{\rho_0}\frac{\partial p}{\partial x_i} = -\frac{\partial u_i u_j}{\partial x_j} + u_i\frac{\partial u_j}{\partial x_j} + \nu_m\frac{\partial}{\partial x_j}\left[\frac{\partial u_i}{\partial x_j} + \frac{\partial u_j}{\partial x_i} - \frac{2}{3}\delta_{ij}\frac{\partial}{\partial x_k}(u_k)\right], \tag{3}$$

Pressure Deviation:

$$\frac{\partial p}{\partial t} + \frac{C_p P}{C_v}\frac{\partial u_i}{\partial x_j} = 0. \tag{4}$$

Although the analytical solution for Beltrami flow assumes incompressible flow, TASS integrates the equations as if compressible. Furthermore, the boundary conditions for the Beltrami simulations are assumed to be periodic on all lateral boundaries, as well as top and bottom boundaries.

3.0 TASS Numerics

This section briefly describes the TASS numerical system. The numerical approximations for momentum and pressure calculation are summarized in table 3.1. Other details of the TASS numerical system can be found in Proctor (1987a) and (1996).

Table 3.1: TASS Numerics

Prognostic Variable	Time Derivative	Space Derivative
Momentum and Pressure	Time-split with small time step for acoustically-active terms and large time step for advection and diffusion; 2nd-order Adams-Bashforth or 1st-order modified Adams-Bashforth	2nd-order Centered, quadratic-conservative differences -- with option for 4th-order accuracy of advection terms

3.1 Time derivative

The time integration in TASS uses a generalized Adams-Bashforth scheme for either second- or first-order approximations (Mesinger 1971), as:

$$Q^{N+1} = Q^{N} + \Delta t\left[(1+\alpha)\left(\frac{\partial Q}{\partial t}\right)^{N} - \alpha\left(\frac{\partial Q}{\partial t}\right)^{N-1}\right], \qquad (5)$$

with the parameter, α, affecting the temporal accuracy. In (5), Q represents any prognostic variable, Δt is the time step. and the superscript N represents the time level. When α is 0.5, (5) represents the second-order Adams-Bashforth scheme (AB). For any other value greater than zero (5) reduces to a first-order scheme.

The AB scheme, while having a second-order truncation error, has a very slight linear amplification error. Mesinger (1971) proposed using a value of 0.809 for α in order to eliminate the amplification error and make the scheme conditionally stable. This value of α gave an optimum range for linear stability, but has a larger phase error and some numerical damping. Equation (5) with a value of 0.6 for α, although having only a first-order truncation error, decreases the linear amplification compared to the AB scheme without introducing significant phase or damping errors. In this report we will use second

order Adams-Bashforth for small time step iterations and (5) with either α=0.5 (AB) or α=0.6 modified Adams-Bashforth (MAB) for large time step integrations.

3.2 Space Derivative

The formulation of the second-order finite difference equations are contained in Proctor (1987a). The fourth-order approximations for the velocity flux and divergence components are in Proctor (1996). The governing equations are approximated on a spatially-staggered three-dimension grid.

3.3 FIlter

Fourth-order filters were designed in TASS to eliminate spurious noise generated by open lateral boundaries and computational noise generated by strong horizontal advection. A modest application of a spatial filter is applied at each time step to eliminate spurious high frequency waves. Filtering in the horizontal plane for u and v velocities is done with a fourth-order biharmonic operator. The equation for the horizontal filtering is:

$$\left.\frac{\partial Q}{\partial t}\right)_{\text{Filter}} = -\frac{\varepsilon}{\Delta t}\left[\Delta x^4 \frac{\partial^4 Q}{\partial x^4} + 2\Delta x^2 \Delta y^2 \frac{\partial^4 Q}{\partial x^2 \partial y^2} + \Delta y^4 \frac{\partial^4 Q}{\partial y^4}\right], \tag{6}$$

where Q is either the u or v velocity and Δx and Δy are the grid sizes in the x and y directions, respectively. The finite difference representation of the biharmonic operator in the bracket is:

$$\begin{gathered} 20Q_{0,0} - 8\,(Q_{1,0} + Q_{0,1} + Q_{-1,0} + Q_{0,-1}) + \\ 2\,(Q_{1,1} + Q_{1,-1} + Q_{-1,1} + Q_{-1,-1}) + \\ (Q_{0,2} + Q_{2,0} + Q_{-2,0} + Q_{0,-2}) \end{gathered} \tag{7}$$

where the subscript refers to the offset from the point (0,0). The first and second terms of the subscript refer to the x and y direction offsets, respectively. Vertical velocity is filtered with a fourth-order filter as:

$$\left.\frac{\partial w}{\partial t}\right)_{\text{Filter}} = -\frac{\varepsilon}{\Delta t}\left[\Delta z^4 \frac{\partial^4 w}{\partial z^4}\right], \tag{8}$$

where w is the vertical velocity, z is the vertical coordinate, and Δz is the grid size in the z

direction. The finite difference representation of the fourth-order derivative is:

$$6w_0 - 4\,(w_1 + w_{-1}) + w_{-2} + w_2\,, \tag{9}$$

where the subscript is the vertical offset from the point (0).

In equations (6) and (8) there is a constant, ε, that modulates the weight of the filter. The ideal choice for this constant will selectively damp spurious high frequency waves while not affecting the actual solution. The effect of the above filters on the accuracy of the simulated Beltrami flow will be evaluated.

4.0 Viscous Beltrami Flow

The following derivation is expanded from Shapiro (1993). Beltrami flow is characterized by the velocity and the vorticity vectors always being aligned in the same direction. This is expressed by the relation

$$\vec{V} \times \nabla \times \vec{V} = 0 \text{ or } \vec{V} \times \vec{\omega} = 0, \tag{10}$$

where $\vec{V}$ is the velocity vector (u,v,w) and $\vec{\omega}$ is the vorticity vector being defined as the curl of the velocity ($\vec{\omega} = \nabla \times \vec{V}$). A brief transformation of the Navier-Stokes equations to the vorticity equations sets the framework in which to derive a particular solution to Beltrami flow. The mass continuity equation and the Navier-Stokes equation for an incompressible viscous flow in cartesian coordinates are:

$$\nabla \bullet \vec{V} = 0, \tag{11}$$

$$\frac{D\vec{V}}{Dt} = -\frac{1}{\rho}\nabla P + \nu \nabla^2 \vec{V} - g\hat{k}, \tag{12}$$

where ρ is the density, ν is the kinematic viscosity, P is the pressure, and g is the acceleration of gravity. The expansion of the material derivative of velocity gives:

$$\frac{\partial}{\partial t}\vec{V} + \nabla\frac{q^2}{2} - \vec{V} \times \nabla \times \vec{V} = -\frac{1}{\rho}\nabla P + \nu \nabla^2 \vec{V} - g\hat{k}, \tag{13}$$

where $q^2 = \vec{V} \bullet \vec{V}$. Substitution of vorticity into (13) gives:

$$\frac{\partial}{\partial t}\vec{V} + \nabla\frac{q^2}{2} - \vec{V} \times \vec{\omega} = -\frac{1}{\rho}\nabla P + \nu \nabla^2 \vec{V} - g\hat{k}. \tag{14}$$

Finally, taking the curl of (14) results in the vorticity equation:

$$\frac{\partial \vec{\omega}}{\partial t} + \vec{V} \bullet \nabla \vec{\omega} - \vec{\omega} \bullet \nabla \vec{V} = \nu \nabla^2 \vec{\omega}. \tag{15}$$

These equations can now be solved based on the limitations of (10) resulting in an exact solution to (12). The alignment of the vorticity and velocity vectors everywhere throughout the flow is written as:

$$\vec{\omega} = \lambda \vec{V}, \tag{16}$$

with λ being a constant. The alignment of vorticity with velocity results in the balancing of the twisting and stretching terms with the non-linear advection terms of (15). The substitution of (16) into (15) yields a diffusion equation for vorticity:

$$\frac{\partial \vec{\omega}}{\partial t} = \nu \nabla^2 \vec{\omega}. \tag{17}$$

Further substitution of (16) into (17) results in a diffusion equation for momentum:

$$\frac{\partial \vec{V}}{\partial t} = \nu \nabla^2 \vec{V}. \tag{18}$$

To further simplify (18), we take the curl of (16) and utilize the vector identity $\nabla \times \left(\nabla \times \vec{V} \right) = \nabla \left(\nabla \bullet \vec{V} \right) - \nabla^2 \vec{V}$ and (16) to arrive at the equation:

$$\nabla^2 \vec{V} + \lambda^2 \vec{V} = 0. \tag{19}$$

Substituting (19) into (18) yields the equation:

$$\frac{\partial \vec{V}}{\partial t} = -\nu \lambda^2 \vec{V}, \tag{20}$$

which has the solution:

$$\vec{V} = \vec{F}(x, y, z)\, e^{(-\nu \lambda t)}, \tag{21}$$

where $\vec{F}$ must satisfy the following Beltrami flow constraints:

$$\nabla \bullet \vec{F} = 0 \text{ and } \vec{F} \times \nabla \times \vec{F} = 0. \tag{22}$$

Now that a solution for the velocity field has been determined, the pressure relation is sought. We apply (16) and (17) into (13) which integrates to:

$$\frac{P}{\rho} + \frac{q^2}{2} + gz = f(t). \tag{23}$$

This equation provides a relation to diagnose pressure once the velocity field has been determined. The results of (21) and (23) are a time varying solution of the incompressible Navier-Stokes equations with constant viscosity. The nature of (21) is a viscous, decaying velocity field. According to Shapiro (1993) a non-trivial solution for Beltrami flow can be obtained only when periodic boundary conditions are assumed.

Furthermore, the pattern of the solution must contain an integral number of wavelengths so that there are no discontinuities across any boundaries. From Shapiro (1993), an exact solution based on (21) that satisfies (22) is:

$$u = -\frac{A}{k^2 + l^2}\left[\lambda l \cos(kx)\sin(ly)\sin(mz) + mk\sin(kx)\cos(ly)\cos(mz)\right] e^{(-\nu\lambda^2 t)}, \quad (24)$$

$$v = \frac{A}{k^2 + l^2}\left[\lambda k \sin(kx)\cos(ly)\sin(mz) - ml\cos(kx)\sin(ly)\cos(mz)\right] e^{(-\nu\lambda^2 t)}, \quad (25)$$

$$w = A\cos(kx)\cos(ly)\sin(mz)\, e^{(-\nu\lambda^2 t)}, \quad (26)$$

with

$$\lambda^2 = k^2 + l^2 + m^2, \quad (27)$$

where A is the maximum magnitude of the vertical velocity. The variation of the wave numbers (k,l,m) can test the ability of a scheme to handle varying gradients of the flow velocities. From (23) the solution for pressure is

$$P = P_s - \rho\left(\frac{u^2 + v^2 + w^2}{2} + gz\right), \quad (28)$$

where P_s is the total pressure at the ground.

5.0 Initialization Conditions for the Validation Case of the TASS Code

The initial conditions are identical to those used in Shapiro (1993), thus allowing comparisons with his numerical simulations using the ARPS model as well as the exact analytical solutions. The following values are used in equations (24) to (28) to initialize the velocity field at time zero:

$A = 2$ m/sec, $L_x = 267$ m, $L_y = 118$ m, $L_z = 44$ m,

$k = 4\pi/L_x$, $l = 2\pi/L_y$, $m = 2\pi/L_z$, $\Delta x = 3$ m, $\Delta y = 2$ m, $\Delta z = 1$ m.

From the initialization conditions given above, the magnitude of the wavenumber is:

$$\lambda = \sqrt{k^2 + l^2 + m^2} = 0.1595 \tag{29}$$

The domain size in the x direction is much longer containing two wavelengths. The other two directions contain one wavelength. The number of points contained in the physical domain for each direction is: $n_x = 89$, $n_y = 59$, and $n_z = 44$. Note that values used for grid size, domain length, and number of points are different in each direction.

Figure 1 portrays the flowfield at the time of initialization and figure 2 shows three-dimensional perspective of velocity vectors at several locations along the East-West axis at initialization.

6.0 TASS Run Results

6.1 Baseline Test Case

A baseline case is chosen which can be compared with both the analytical Beltrami solution and the ARPS code. The baseline case assumes ν=1 m^2/sec, the second order AB time differencing scheme, and second-order space derivatives. The analytical time history of the maximum velocity components and the sum of the kinetic energy for this case is shown in figure 3. After 82 seconds the velocity magnitude has decayed to 12% of its initial value and the kinetic energy is 1% of its initial value. The fourth-order filter coefficient in TASS (see equations (6) through (9)) was set to ε=1.52x10^{-3}. The large and small time steps in TASS are automatically chosen based on linear stability criteria, with the value being 0.058 and 0.0012 seconds, respectively. The simulation took 36 minutes of central processing unit (CPU) time on a Cray C90 supercomputer.

6.1.1 Comparison of TASS with ARPS

ARPS is a second-order spatial and temporal accurate code, which, like TASS, splits the time integration into large and small time steps. ARPS uses an Asselin time filter to suppress the development of nonlinear instability due to the leap-frog time differencing scheme. The large and small time steps used in the ARPS simulation were 0.19 and 0.002 seconds, respectively (Shapiro 1993). Timing was unavailable for this simulation.

The method of evaluating the relative performance will be the use of both contour and vector plots of the velocity error for horizontal cross-sections. The error values are

computed from the following relation:

$$V_{err} = V_{MODEL} - V_{ANL} \tag{30}$$

where V is the particular velocity component.

A comparison between the TASS Baseline case and ARPS error fields at the horizontal plane $mz = \pi/2$ (z=10 meters) is shown in figures 4 and 5. The TASS and ARPS error vectors (figure 4) are both plotted on the same scale showing that TASS has a significantly smaller error magnitude. At this time the value for the maximum error for U and V velocities in the TASS flowfield are 0.005145 and 0.004662 m/sec, respectively, with the maximum U and V velocity being approximately 1.0 m/sec. Figure 5 shows the maximum absolute vertical velocity error of TASS is less than half that of ARPS. The maximum TASS vertical velocity error domain-wide is 0.004457 and the maximum vertical velocity is about 0.75 m/sec.

6.2 Additional TASS Runs

Additional runs are made with TASS to evaluate its accuracy for: 1) second- vs fourth-order finite differencing for spatial advection, 2) modification to the time differencing scheme, and 3) sensitivity to the fourth-order numerical filter.

These additional TASS runs will be evaluated primarily based on two variables, which are based on percentage error. The first is the kinetic energy error and the second is the vertical velocity error. The kinetic energy error is obtained by first calculating the exact analytical Beltrami solution. Next the kinetic energy over the entire domain for both the analytical and TASS fields are then determined. The error is computed by the percentage error of the two resulting numbers as given by the equation:

$$\%KE_{ERR} = \left(\frac{KE_{MODEL} - KE_{ANL}}{KE_{ANL}} \right) 100 \quad . \tag{31}$$

This error gives an indication of amount of numerical diffusion. The next variable is the vertical velocity error and is computed by the following equation:

$$Error_{RMS} = \left(\frac{Max_{i,j,k}(|W|_{MODEL}) - Max_{i,j,k}(|W|_{ANL})}{Max_{i,j,k}(|W|_{ANL})} \right) 100 \, , \tag{32}$$

where $Max_{i,j,k}(|W|)$ is the maximum vertical velocity over the entire domain. This variable will give an indication of the error in the rate of change in the maximum vertical velocity. These two diagnostic error variables are evaluated over the course of the time integration.

Two sets of simulations are conducted with the first set having a larger value of viscosity and the second set a relatively small value. With a large value for the viscosity the peak magnitude of the velocity decays with time. Therefore, the time integration accuracy along with the advection terms and the coupling between the pressure and the velocity fields are important for an accurate simulation. On the other hand, for small viscosity as in the second set of experiments, the flow becomes nearly steady state, or weakly decaying, and the accuracy of the time integration is less critical. In this set, the accuracy of spatial advection and proper coupling between pressure and velocity are critical to the success of the simulation. The value of viscosity chosen for each of these two sets are 1.0 and 0.01 m^2/sec, representing decaying and weakly-decaying cases, respectively. For the weakly-decaying case, the velocity and the kinetic energy are 98% and 96%, respectively, of their original values at 82 seconds of simulation time.

Table 6.1 shows the settings for all TASS runs and table 6.2 shows the error values at the end of each run. The first six runs are the decaying case (ν=1 m^2/s) and the remaining five are the weakly decaying case (ν=0.01 m^2/s). The baseline case used in section 6.1 is run number 5. Table 6.1 is shaded to aid in locating the runs compared. Similarly shaded cells within each case and setting represent comparison runs to be discussed. For each comparison the remaining settings are unchanged, thereby isolating the effect of the setting in question. For example, the decaying case has two comparisons for spatial accuracy with one set using the AB scheme (runs 3 and 5) and the other using the MAB scheme (runs 1 and 2), and the fourth order filter coefficient being constant for both sets. The results of all the runs are very good with the maximum kinetic energy error level being less than 0.5% demonstrating that the TASS core formulation is stable and has very little numerical dissipation. The time history of the errors for the decaying case are shown in figure 6 with the differences between the first five runs being relatively slight. The slope of the kinetic energy error for these five runs shows the decay of the TASS simulation to slightly lag the analytical solution. The weakly-decaying case error history has all but one run having a negative slope (figure 7). The line patterns of runs with the same settings for the two cases are the same in figures 6 and 7 to further aid in comparison.

Table 6.1: TASS Settings

	Run #	Spatial Accuracy	Time Integration Scheme	Fourth Order Filter Coeff.
Decaying Case Runs	1	4th	MAB	1.52×10^{-3}
	2	2nd	MAB	1.52×10^{-3}
	3	4th	AB	1.52×10^{-3}
	4	4th	MAB	1.8×10^{-3}
	5	2nd	AB	1.52×10^{-3}
	6	4th	MAB	$3. \times 10^{-3}$
Weakly Decaying Case Runs	7	4th	MAB	1.52×10^{-3}
	8	4th	MAB	0
	9	4th	AB	1.52×10^{-3}
	10	4th	MAB	1.81×10^{-3}
	11	2nd	MAB	1.52×10^{-3}

Table 6.2: TASS Results

	Run #	Percent Error at 82 seconds	
		Kinetic Energy	Vertical Velocity
Decaying Case Runs	1	.346	.180
	2	.344	.403
	3	.284	.150
	4	.275	.146
	5	.285	.372
	6	-.029	-.003
Weakly Decaying Case Runs	7	-.38	-.283
	8	.0053	-.101
	9	-.38	-.283
	10	-.45	-.308
	11	-.43	-3.11

6.2.1 Spatial Accuracy

The spatial advection in TASS is approximated by a quadratic conservative central difference scheme, with an option for either second- or fourth-order differencing. The important result from the spatial accuracy comparison will be the additional CPU time required as compared to the benefits of fourth-order spatial advection.

The four runs that isolate the effect of spatial accuracy for the decaying case are runs 1 and 2 and runs 3 and 5. The first pair utilize the MAB time integration scheme with the latter pair using the AB scheme. The runs that are fourth-order spatially accurate are runs 1 and 3. The filter coefficient for these runs is set at 1.52×10^{-3}. For these two comparisons, the change in advection accuracy has negligible effect on the kinetic energy error (figure 6). However, the relative differences are noticeable for the vertical velocity error, with the error for fourth-order spatial advection being less than half that of second-order. Figures 8 and 9 display TASS results for runs 3 and 5. The fourth-order horizontal velocity error vectors (figure 8) are substantially smaller than the second-order vectors and a comparison of the magnitude of the vertical velocity error shows the fourth-order run to be less than one-fifth the magnitude of the second-order run (figure 9). The velocity error vectors also show the pattern for the two runs to be substantially different, whereas the vertical velocity plots show the same pattern. The increased computer time required for the fourth-order scheme is small, being less than 6% greater than the second-order run.

For the weakly-decaying case, runs 7 and 11 isolate the spatial accuracy effect. For these runs the filter coefficient is set at 1.52×10^{-3} and the time integration is the MAB

scheme. Run 7 is the fourth-order spatial accurate run. The spatial accuracy has a much greater effect in this case. The reduction of the error is about 13% for the kinetic energy error and an order of magnitude for the vertical velocity error (figure 7). Further, the second-order advection, run 11, shows a nonlinear error growth near the end of the run with the strongest divergence from the analytical solution being most apparent in the vertical velocity error. The additional CPU time required for this case is less than 5%. The larger values for the error levels is not unexpected since the weakly-decaying case emphasizes the advection terms.

The important observations from the effect of the spatial accuracy is a noticeable improvement in the quality of the solution for fourth-order spatial accuracy with little additional CPU time required for both cases. The importance of spatial accuracy is quite apparent for vertical velocity error for the weakly-decaying case. For the decaying case, the differences resulting from a change of spacial accuracy is not as obvious from the kinetic energy and vertical velocity error histories, but the contour and vector error plots display quite a large dependence upon this change. The additional CPU time required for the additional accuracy is on average for all runs only 4.6%. Further, the added percent of CPU required for the fourth-order spatial advection will be reduced as additional parts of the simulation system are activated (i. e. turbulence or microphysics parameterization modules).

6.2.2 Temporal Accuracy

The objective of this part of the investigation is to determine if the MAB can be used as an alternative time integration scheme.

The four runs that isolate the effect of the temporal accuracy for the decaying case are runs 1 and 3 and runs 2 and 5. The spatial accuracy of the first two are fourth order and the others are second order with the filter coefficient being set at 1.52×10^{-3}. Runs 3 and 5 use the AB scheme. The increased error due to the MAB scheme (runs 1 and 2) is relatively small (22%) for the kinetic energy error values and non-existent for the vertical velocity error (figure 6). Figures 10 and 11 compare TASS results for runs 1 and 3. Unlike the spatial accuracy comparison, the differences are quite small for this comparison, and the flow patterns are essentially the same (figure 10). The comparison of the maximum vertical velocity error values show the relative improvement of the AB over the MAB time scheme to be only 8% (figure 11). Therefore, although the error variables indicate a higher lever of error resulting from the MAB scheme, the plots show much less impact upon the quality of the solution.

The runs that examine the effect of the two time differencing schemes for the weakly-decaying case are 7 and 9. Both runs are fourth-order spatial accurate with the filter coefficient set at 1.52×10^{-3}. Run 9 uses the AB scheme. Both kinetic energy and vertical velocity errors for this case are identical (figure 7).

The result of this comparison will be taken only from the decaying case because the weakly-decaying case shows no sensitivity to either time differencing scheme. The time history results show increased error only in the kinetic energy error with the contour and vector error plots showing no differences. The lack of significant differences shows that the phase or damping errors of the MAB scheme are so slight that they do not adversely affect the quality of the solution. Thus for Beltrami flow, both the AB and MAB

schemes give comparable results, with the AB scheme being slightly more accurate.

6.2.3 Fourth-Order Filter

The fourth-order filter is controlled by the coefficient, ε, from equations (6) and (9). The values used result in modest to no filtering. Moderate and large values are avoided since they can result in over smoothing of the solution and non-physical damping of the kinetic energy. The effect of this coefficient on the simulation results will be evaluated.

The effect of this coefficient for the decaying case is examined in runs 1, 4, and 6. These runs assume fourth-order spatial accuracy and the MAB time integration scheme. Run 6 has the greatest filtering and run 1 has the least. The trend is a decrease of the error slope with an increasing filter value for both the kinetic energy and vertical velocity errors (figure 6).

The weakly-decaying simulations also use the MAB scheme and fourth-order space derivatives. Runs 7, 8, and 10 demonstrate the effect that the fourth-order filter coefficient has upon the solution, with run 7 having no filtering and run 10 having the most. The trends are the same as that of the decaying case for the kinetic energy error with increasing filter values decreasing the slope of the error growth (figure 7). For no filtering, the vertical velocity error shows better accuracy during the first minute of the simulation. The other two runs show no appreciable difference due to filtering.

The important conclusion from the cases examining the sensitivity of the fourth-order filter is that all settings gave very good results. However, small values for ε had the effect of reducing the slope of the error growth.

6.2.4 Comparison of ARPS to TASS with Fourth-Order Spatial Accuracy

Run 3 is the same as ARPS with the exception of spatial accuracy being fourth order. The fourth-order spatial advection results of TASS are an order of magnitude better than ARPS (figure 12). Although not a fair comparison to ARPS, this shows the relatively high degree of accuracy possible with TASS.

7.0 Conclusion

The Beltrami flow constraint on viscous incompressible flow results in an exact solution to the Navier-Stokes equations. The structure of Beltrami flow is a complex, stationary, viscous, decaying, vortical flow. This solution is capable of verifying the core numerics of any 3-D computational fluid dynamics code in the absence of turbulence, moisture, and buoyancy effects. TASS has been modified to simulate the Beltrami flow field, testing the accuracy of the core numerics of the code. The results presented here have shown that TASS is capable of simulating Beltrami flow with extremely small errors. The TASS code has demonstrated accuracy in comparison to both an exact solution and other numerical results. The conclusion from an accuracy analysis of TASS show that fourth-order spatial accuracy with Adams Bashforth time integration and a fourth-order filter coefficient value of 1.52×10^{-3} gives the best results for either strongly- or weakly-decaying 3-D vortical systems. Of these three areas, the most significant is the order of spatial accuracy with the added cost of running the fourth order vs second order being at most only 6%. The conclusion from the comparison of the time differencing schemes is that negligible difference occurs between the AB and MAB scheme. The accuracy of the solution can be improved further by a modest application of a fourth-order filter without detriment to the quality of the solution. TASS gives stable results with minimal numerical diffusion and is in excellent agreement with the analytical solution. The results of the Beltrami flow simulations suggest that TASS is capable of accurately simulating non-linear and time-varying vortical flow fields with almost no artificial dissipation.

Acknowledgments

This work was performed for the National Aeronautics and Space Administration under contract NAS1-18925. The work was performed at the Langley Research Center with Dr. Fred Proctor of the Crew Systems and Operations Branch as the contract monitor. The computations were carried out on the NASA Langley and Ames supercomputers.

8.0 References

Mesinger, F., 1971: Numerical Integration of the Primitive Equations with a Floating Set of Computation Points: Experiments with a Barotropic Global Model. Monthly Weather Review, 99, pp 15-29.

Proctor, F. H., 1987a: The Terminal Area Simulation System, Volume I: Theoretical formulation. NASA Contractor Report 4046, NASA, Washington, DC, p 176. [Available from the National Technical Information Service, Springfield, VA, 22161.]

Proctor, F. H., 1987b: The Terminal Area Simulation System, Volume II: Verification Experiments. NASA Contractor Report 4047, NASA, Washington, DC, p 112. [Available from the National Technical Information Service, Springfield, VA, 22161.]

Proctor, F. H. and R. L. Bowles, 1992: Three-dimensional Simulation of the Denver 11 July 1988 Microburst-producing Storm. Meteorological. and Atmosphere Physics, 47., pp 107-124.

Proctor, F. H., 1993: Case Study of a Low-reflectivity Pulsating Microburst: Numerical Simulation of the Denver, 8 July 1989, Storm. To appear in Preprints, 17th Conference on Severe Local Storms, St. Louis, American Meteorological Society, pp 677-680.

Proctor, F. H., E. M. Bracalente, S. D. Harrah, G. F. Switzer, and C. L. Britt, 1995: Simulation of the 1994 Charlotte Microburst with Look-Ahead Windshear Radar. 27th Conf. on Radar Meteorology, Vail, CO, American Meteorological Society, pp 530-532.

Proctor, F. H. 1996: Numerical Simulation of Wake Vortices Measured During the Idaho Falls and Memphis Field Programs. 14th AIAA Applied Aerodynamics Conference, New Orleans, LA, Paper No. 96-2496

Schowalter, D. G., D. S. DeCroix, Y.-L. Lin, F. H. Proctor, S. P. Arya, and M. L. Kaplan, 1995: Turbulent Statistics in the Atmospheric Boundary Layer: a Comparison of Large Eddy Simulation with Observations. Preprints, 11th Symposium on Boundary Layers and Turbulence, Charlotte, NC, American Meteorological Society, 1995, pp 552-555.

Schowalter, D. G., D. S. DeCroix, Y.-L. Lin, S. P. Arya, and M. Kaplan, 1996: Planetary Boundary Layer Simulation Using TASS. NASA Contractor Report 198325.

Shapiro, Alan, 1993: The Use of an Exact Solution of the Navier-Stokes Equations in a Validation Test of a Three-Dimensional Nonhydrostatic Numerical Model. Monthly Weather Review, Vol 121, pp 2420-2425.

Taylor, G. I., 1923: On the Decay of Vortices in a Viscous Fluid. Phil. Mag., 46, pp 671-674.

Wang, C. Y., 1990: Exact Solutions of the Navier-Stokes Equations -- The Generalized Beltrami Flows, Review and Extension. Acta Mechanica, 81, pp 69-74.

9.0 Figures

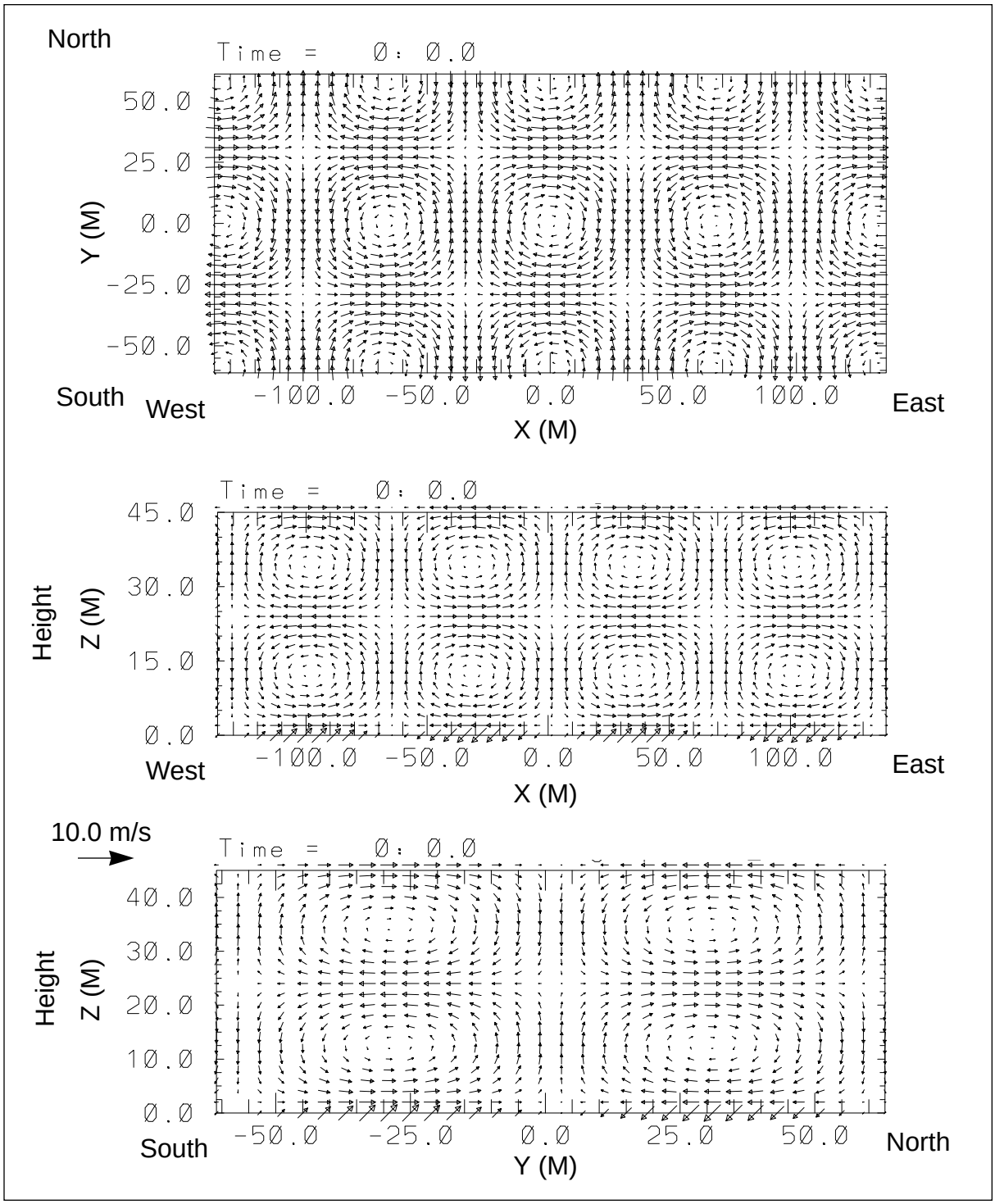

Figure 1: Initial Beltrami flow field 2-D vector plots. Horizontal plane at mz = π/2 (top), vertical East-West Plane at ly = π (middle), and vertical North-South plane at kx = π (bottom).

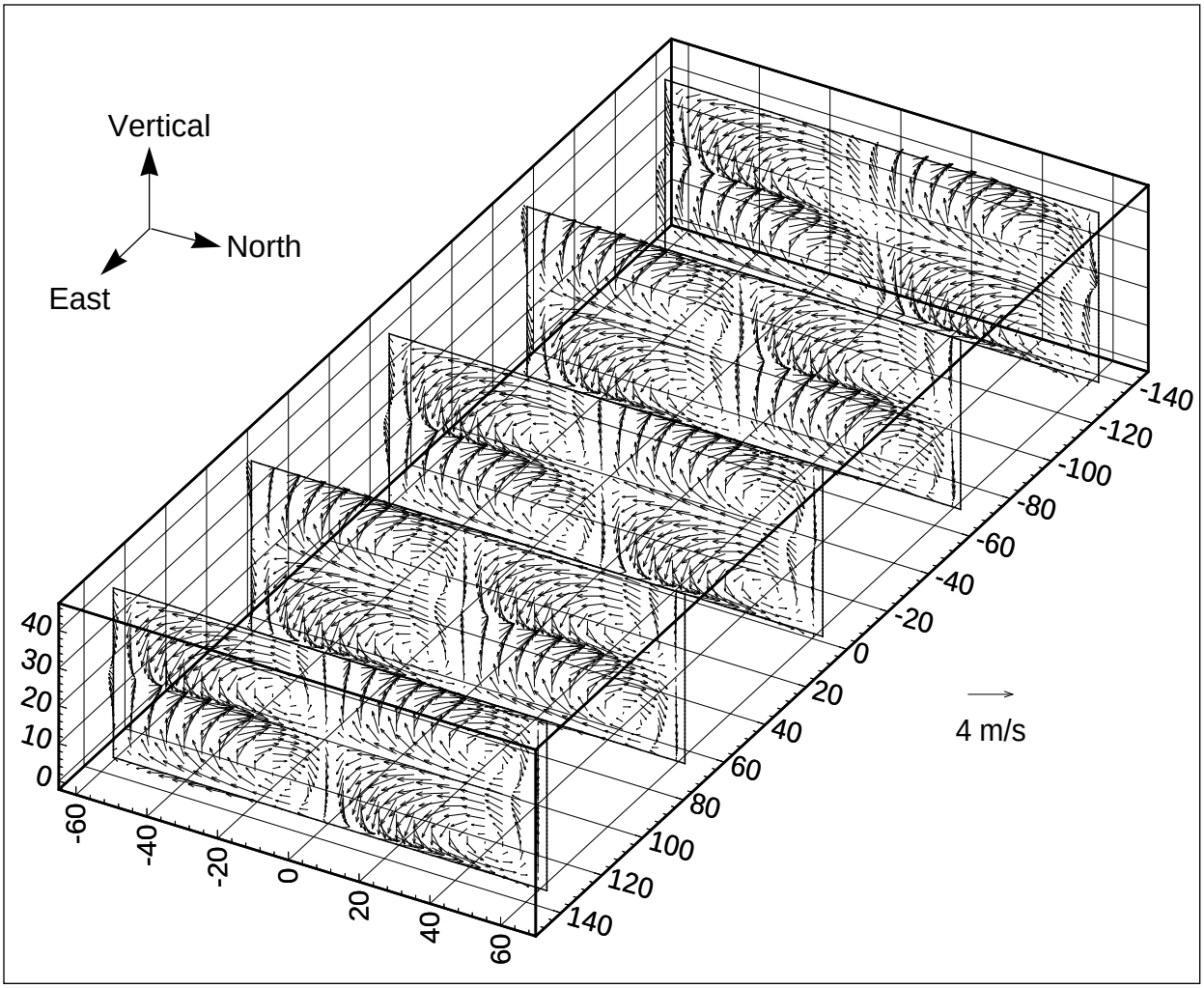

Figure 2: Perspective of North-South vertical planes of vectors at kx = 0,π,2π,3π and 4π.

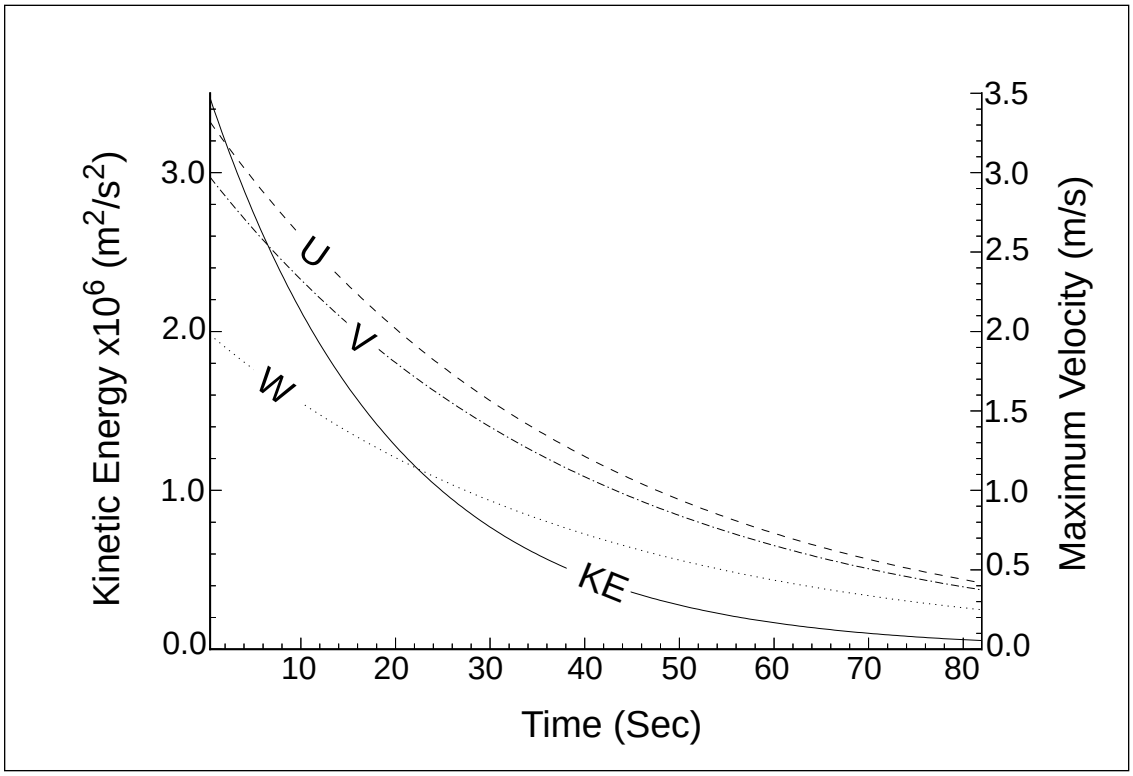

Figure 3: Analytical time history of total kinetic energy and maximum velocity for viscously decaying Beltrami flow (ν=1 m^2/s).

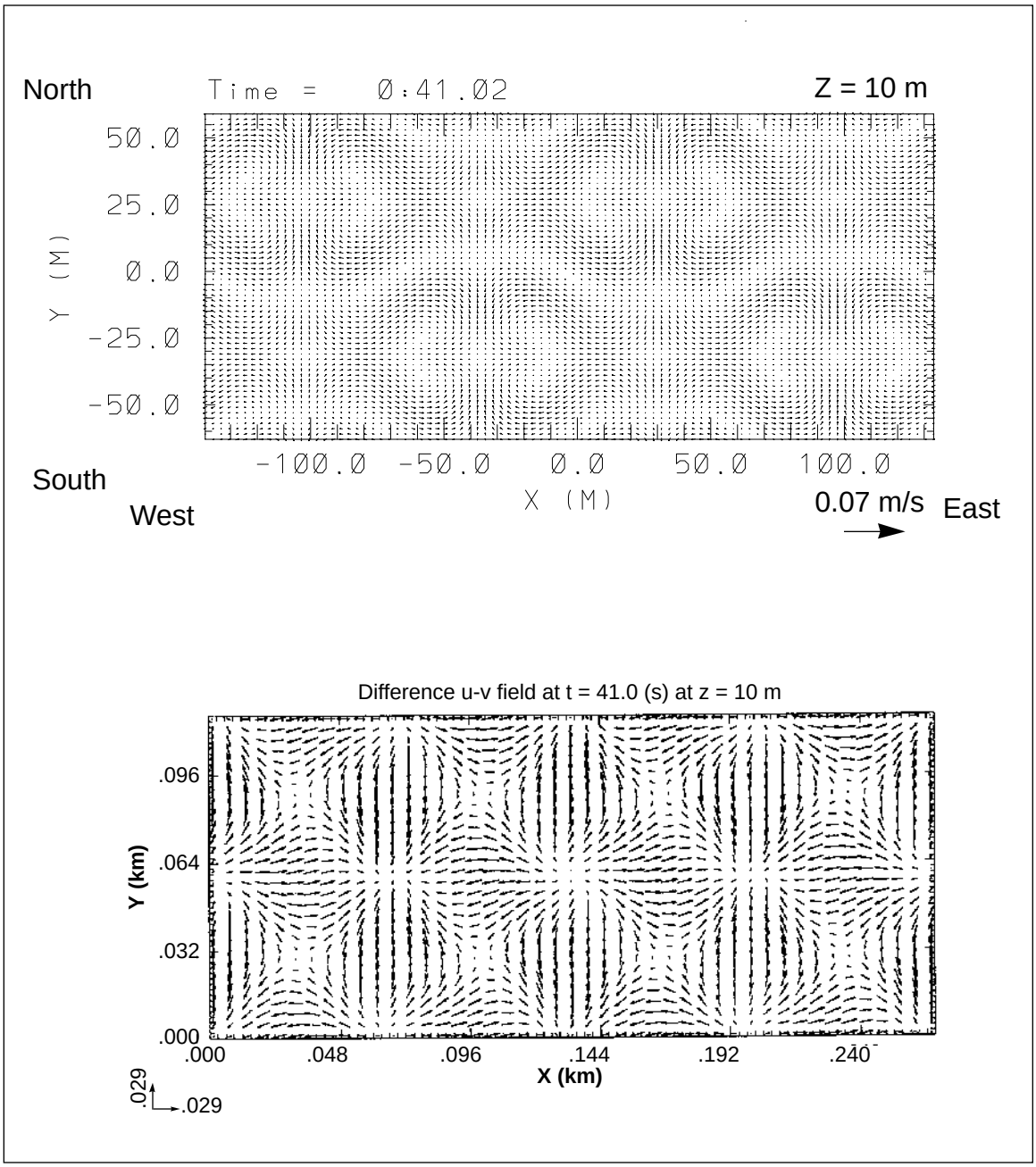

Figure 4: Comparison of TASS (top) and ARPS (bottom) horizontal velocity error plots at mz = π/2.

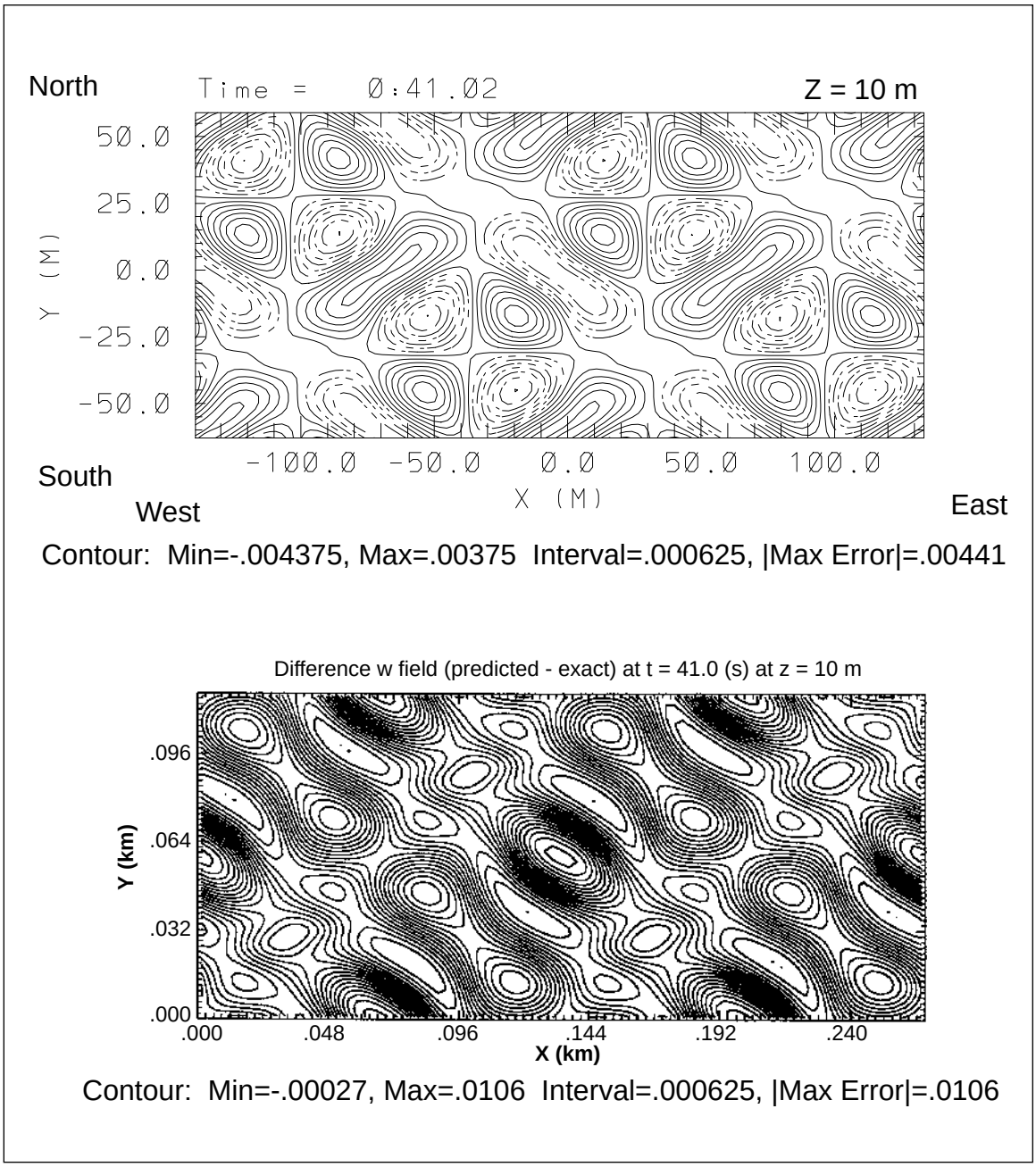

Figure 5: Comparison of TASS (top) and ARPS (bottom) horizontal vertical velocity error contour plots at mz = $\pi/2$.

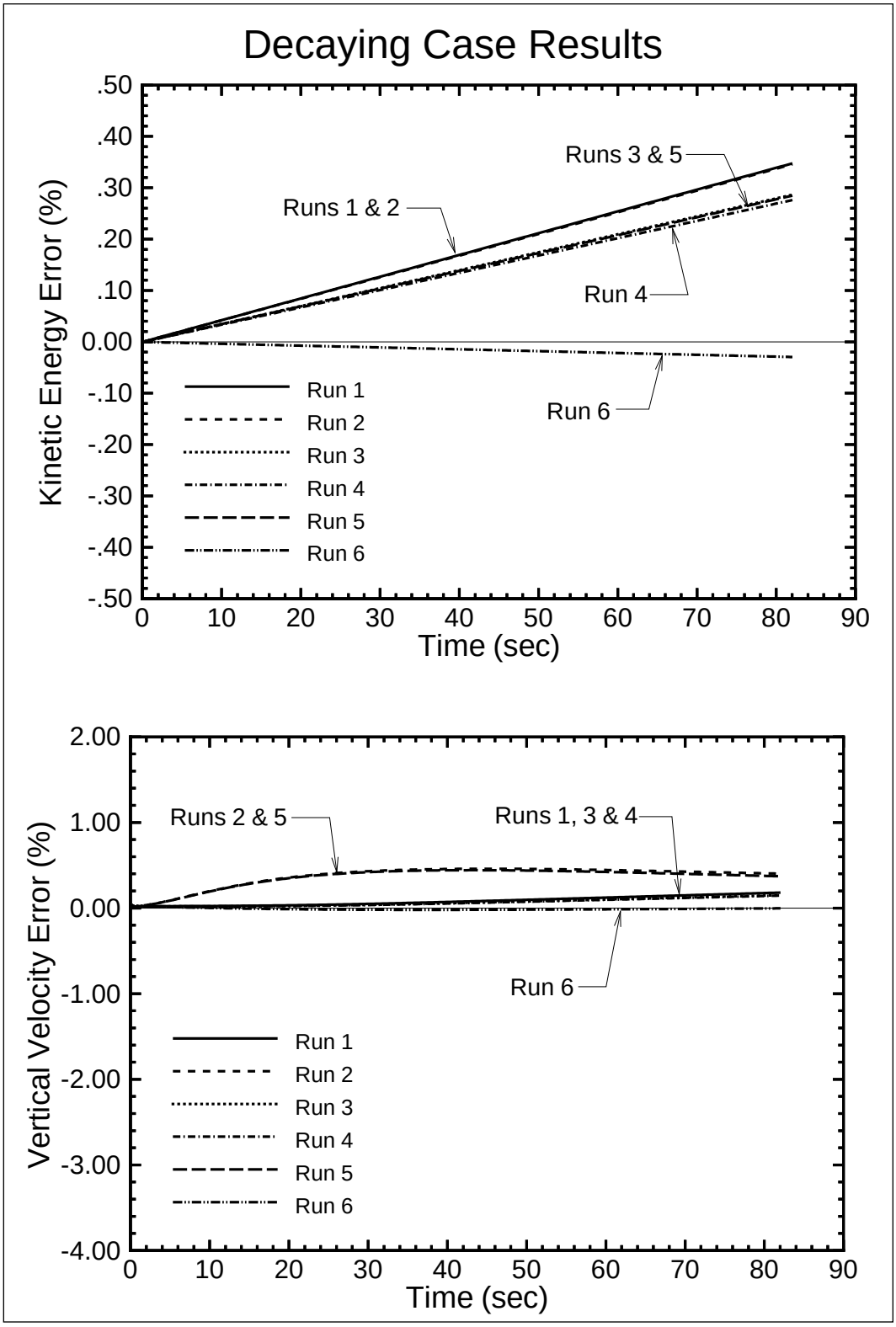

Figure 6: Time history of kinetic energy (top) and vertical velocity (bottom) percent error for the decaying case.

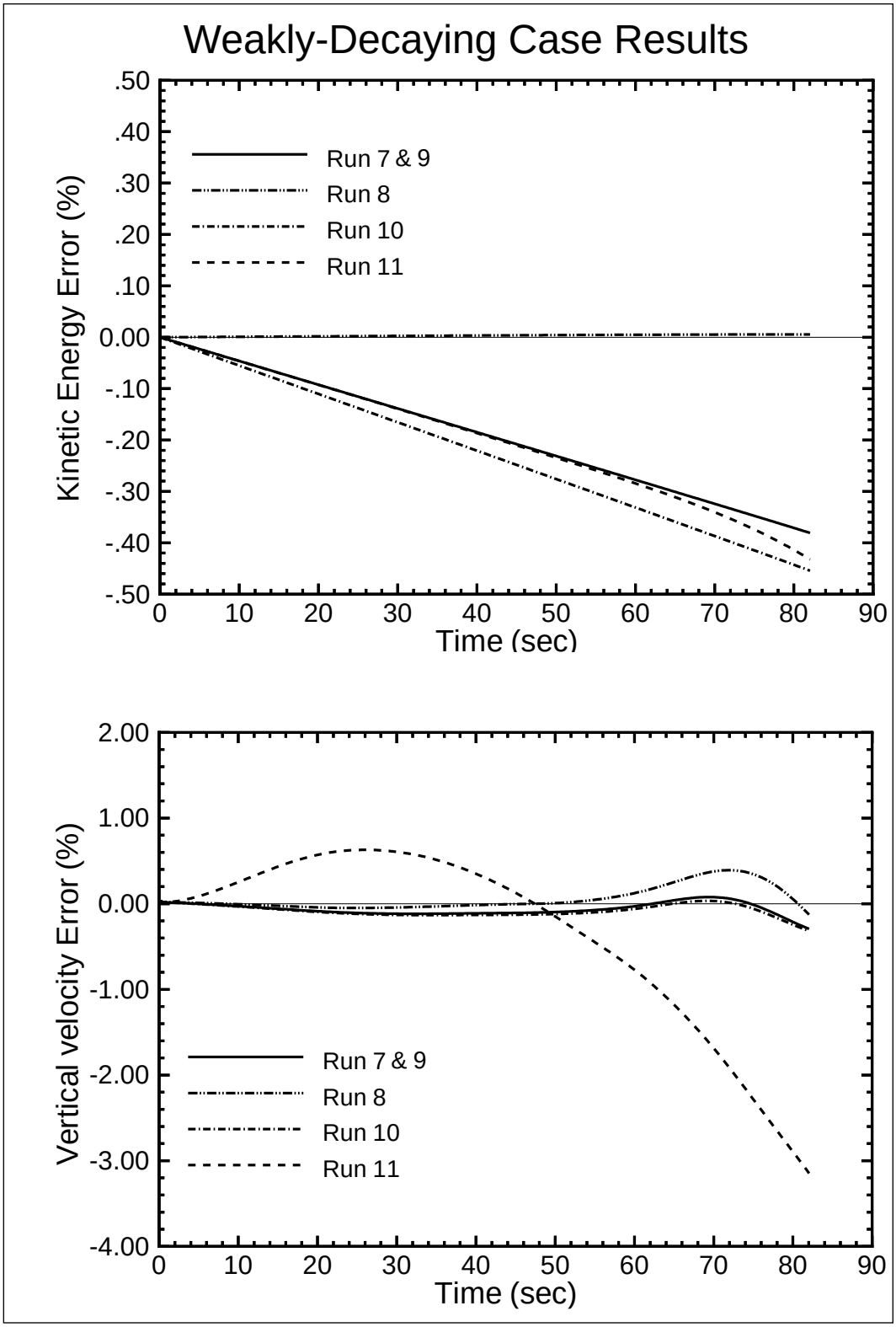

Figure 7: Time history of kinetic energy (top) and vertical velocity (bottom) percent error for weakly-decaying case (runs 7 and 9 are identical).

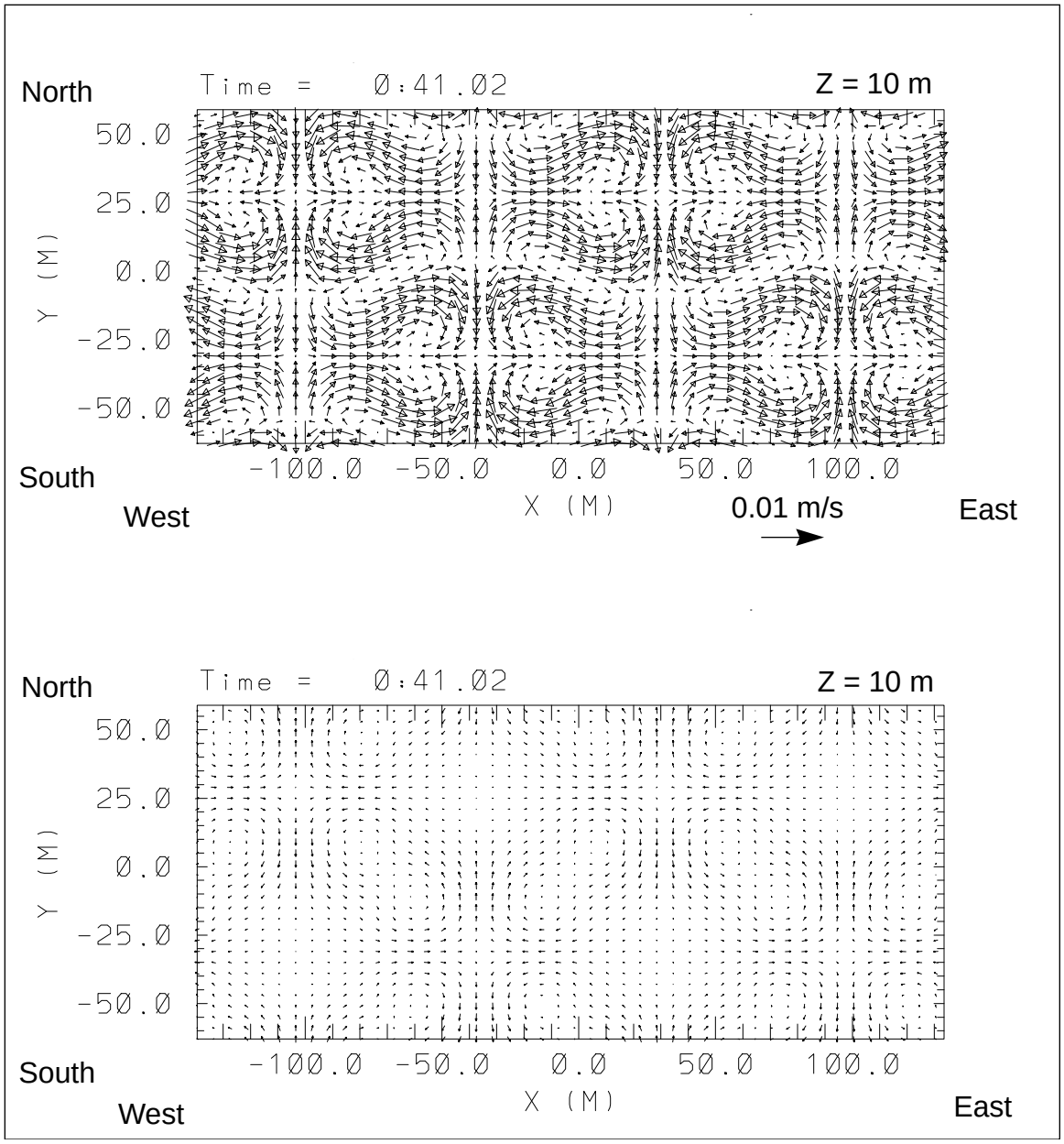

Figure 8: Spatial second-order (top) and fourth-order (bottom) horizontal TASS velocity error vector plots at mz = π/2.

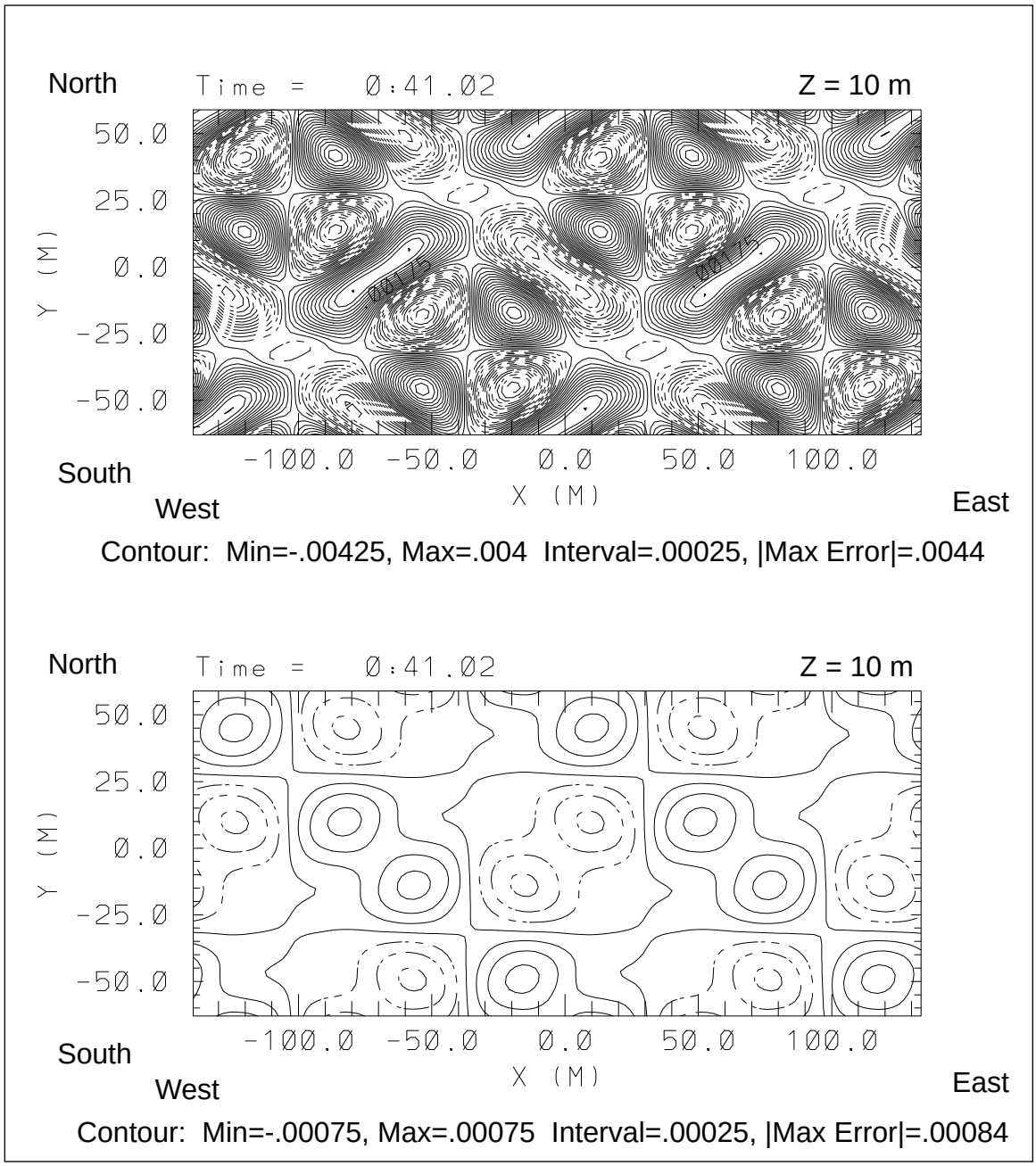

Figure 9: Spatial second-order (top) and fourth-order (bottom) horizontal TASS vertical velocity error contour plot at mz = $\pi/2$.

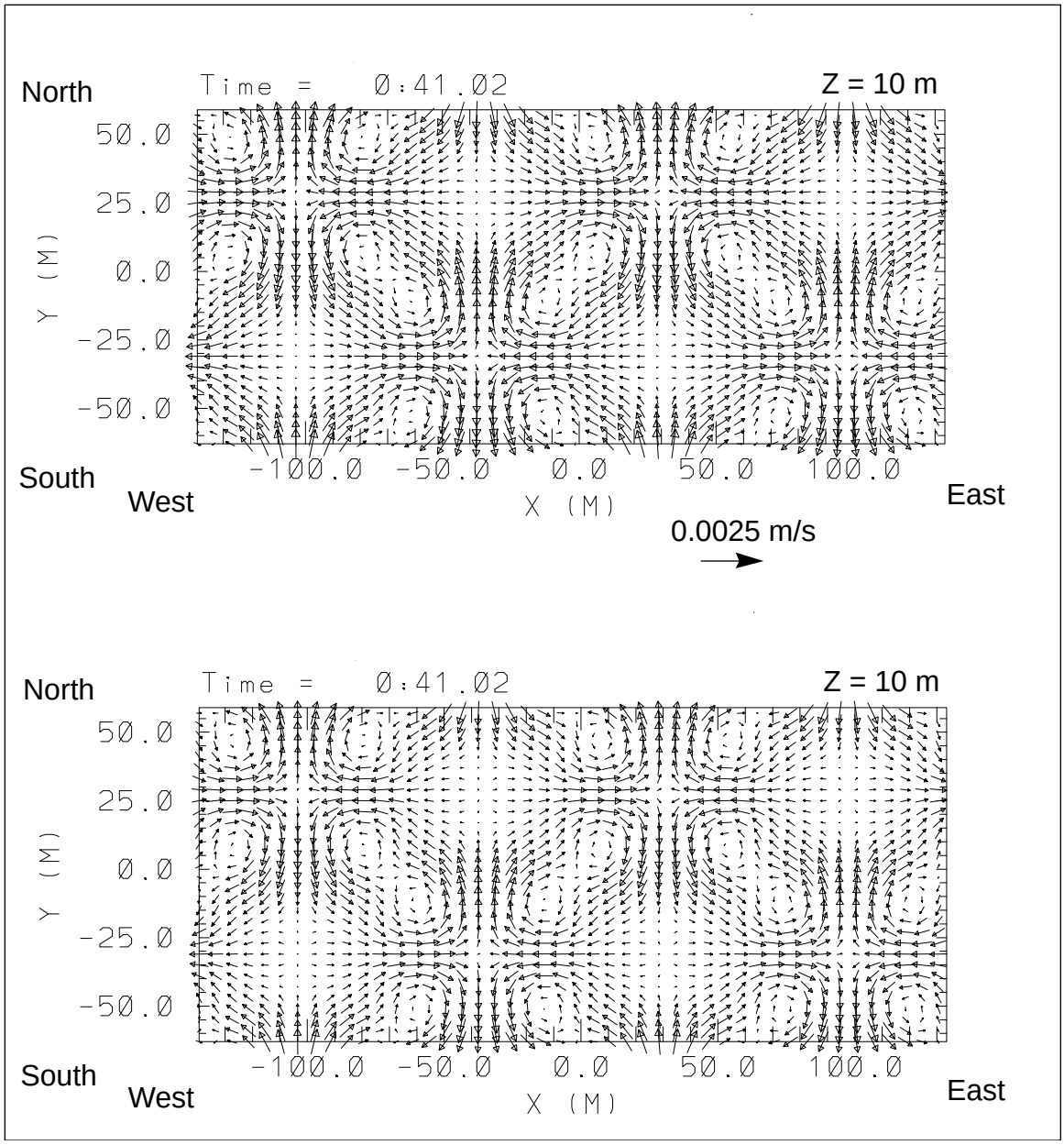

Figure 10: Temporal MAB scheme (top) and AB scheme (bottom) horizontal TASS velocity error vector plot at mz = π/2.

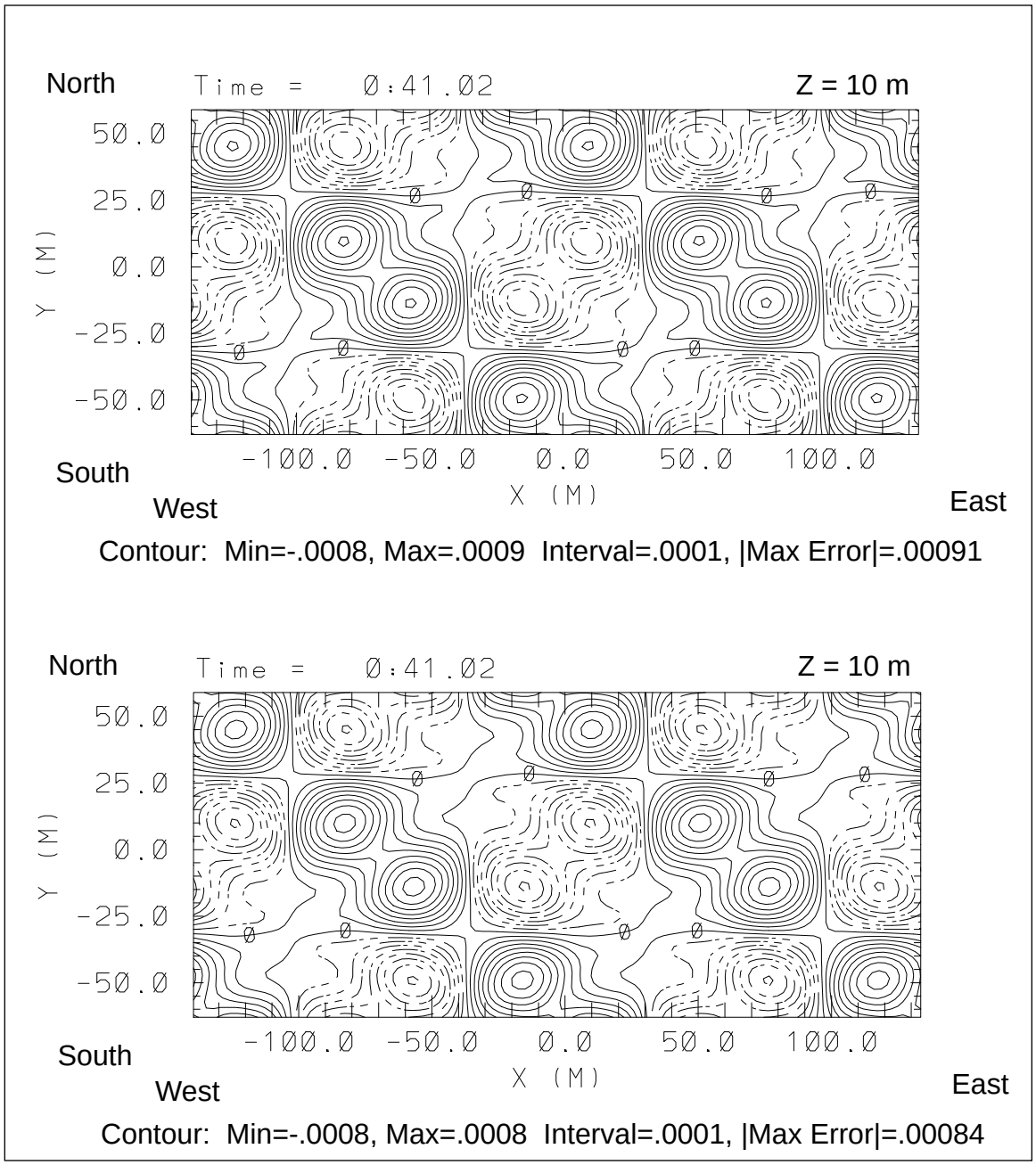

Figure 11: Temporal MAB scheme (top) and AB scheme (bottom) horizontal TASS vertical velocity error contour plot at mz = $\pi/2$.

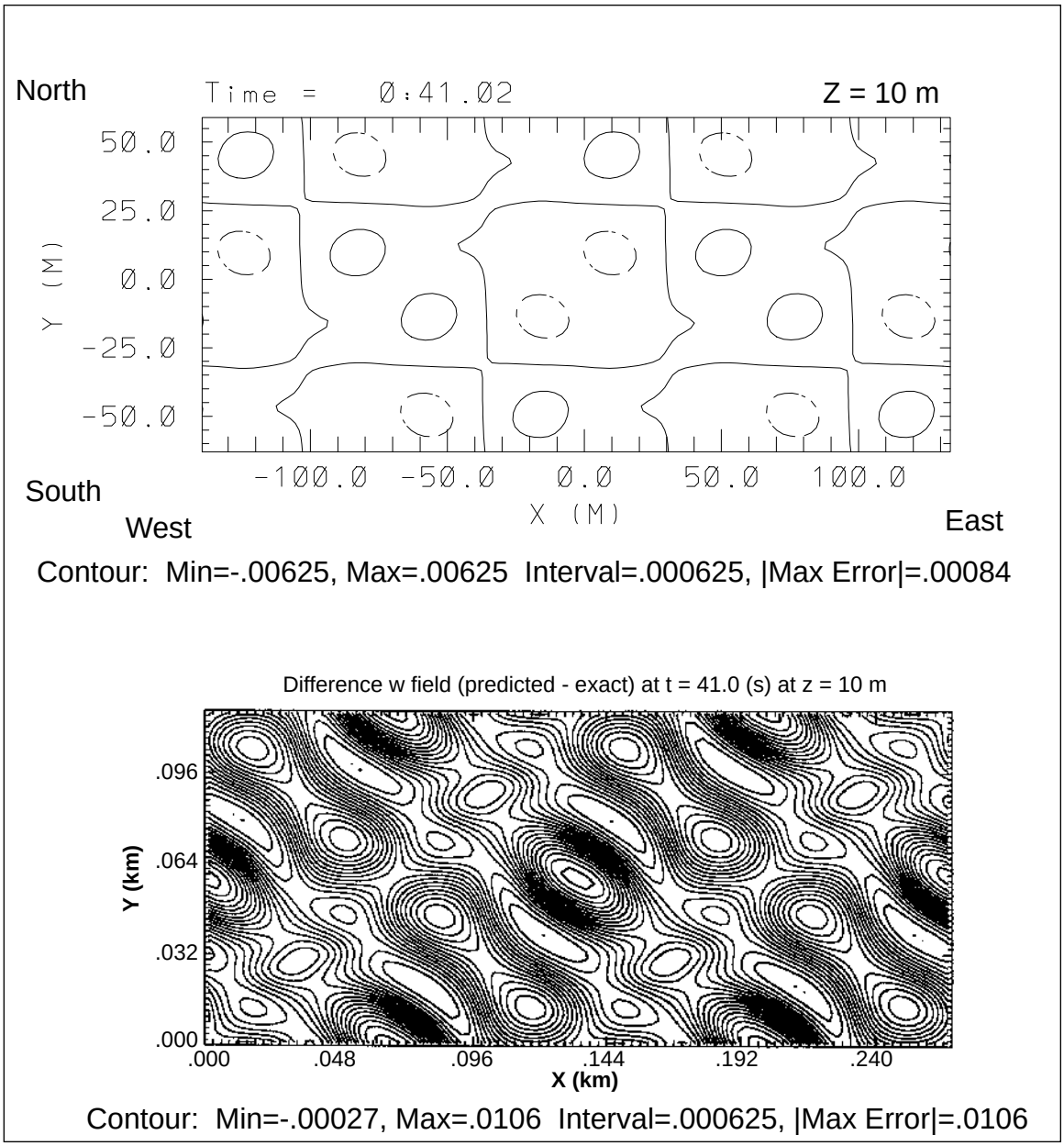

Figure 12: Horizontal vertical velocity error contour plot at mz = $\pi/2$ for TASS with fourth-order spatial advection (top) and ARPS (bottom).